

Ultrasonic defect characterization using time-domain scattering matrices and convolutional sparse coding

Long Bai, Nanxin Liu, Changrong Guo, Jianfeng Xu ^{*}

State Key Laboratory of Digital Manufacturing Equipment and Technology, School of Mechanical Science and Engineering, Huazhong University of Science and Technology, Wuhan, 430074, China



ARTICLE INFO

Keywords:
 Defect characterization
 Scattering matrix
 Convolutional sparse coding
 Rough cracks
 Volumetric defects

ABSTRACT

In this paper, the use of the time-domain scattering matrix for ultrasonic characterization of defects is explored. An approach based on convolutional sparse coding is proposed for extraction of the shift-invariant features of the time-domain scattering matrix. The results of a simulation show that the proposed approach can be reliably used for classification of the rough cracks. In addition, the mean sizing error and its standard deviation are also reduced compared with the use of the frequency domain scattering matrix. In experiments, a 1.5 mm slot and 1.5 mm elliptical defect were sized to within 0.25 mm using a 2.5 MHz, 64 element linear array with an element pitch of 0.5 mm. Excellent sizing results were obtained for inclined slots with a large orientation angle (*i.e.* 60°).

1. Introduction

The presence of a defect (*e.g.* a crack) can often lead to the failure of a structural component, and accurate detection and characterization of defects are crucial to ensure the safety of such components. Ultrasonic testing (UT) [1] is among the most widely used techniques in the field of non-destructive evaluation (NDE) [2]. For example, it can be applied to inspection of rails [3], pipelines [4], nuclear power plants [5], and additive manufactured components [6]. Ultrasonic A-scan signals measured by a transducer probe can be used to assess whether the component contains a defect (*e.g.* by comparing the signal amplitude to a fixed threshold [7]). In addition, the size of a crack-like defect can also be deduced from A-scan signals by adopting amplitude-based sizing (*e.g.* the 6-dB drop approach [8]) or the time-of-flight diffraction (TOFD) method [9]. Ultrasonic array imaging [10] is another important technique which can be adopted for detection and defect sizing. Zhang et al. proposed a 6-dB box fitting approach for sizing crack-like defects [11] based on the total focusing method (TFM) [12]. Camacho et al. combined the TFM and phase coherence imaging (PCI) for more robust crack sizing and applied this approach to online monitoring of fatigue cracks [13]. For imaging of unknown anisotropic materials, Ménard et al. adopted a gradient ascent algorithm and optimized the TFM calculations iteratively [14]. A similar idea can also be found in Ref. [15], where Lin et al. proposed a model-based approach for determining time delays in multidirectional CFRP laminates.

The capability of a modern UT system to detect and characterize defects can be significantly improved considering the recent development of artificial intelligence and deep learning techniques. The convolutional neural network (CNN) [16] is a representative deep learning model which has been adopted for both classification [17] and regression (*i.e.* defect characterization [18]) tasks. For example, Pyle et al. simulated image datasets for training using a hybrid model of wave scattering, and used the trained CNN model to characterize real defects [19]. Munir et al. has developed a two-step classification procedure in which noisy input data (ultrasonic A-scans measured by varying the probe angle) are first processed by a deep neural network known as autoencoder and then classified by a CNN [20]. In addition, feature extraction and feature selection have been studied by many researchers in the NDE community. Cruz et al. combined the discrete Fourier, wavelet, and cosine transforms for feature extraction and adopted principal component analysis (PCA) [21] for feature selection [22]. The features were then used to train a multilayer perceptron neural network for defect detection in steel welded joints [22]. In Ref. [23], a dynamic defect classification system which performs feature selection based on estimation of the local classification accuracy has been developed. The application of novel classifiers can also be found in the literature: for example, one-class classification algorithm for defect detection in wind turbine blades [24] and optimized softmax classifier for accurate classification of A-scan signals with similar curves [25].

Despite the improvements achieved in the application of advanced

* Corresponding author.

E-mail addresses: bailong@hust.edu.cn (L. Bai), 834788987@qq.com (N. Liu), d202180271@hust.edu.cn (C. Guo), jfxu@hust.edu.cn (J. Xu).

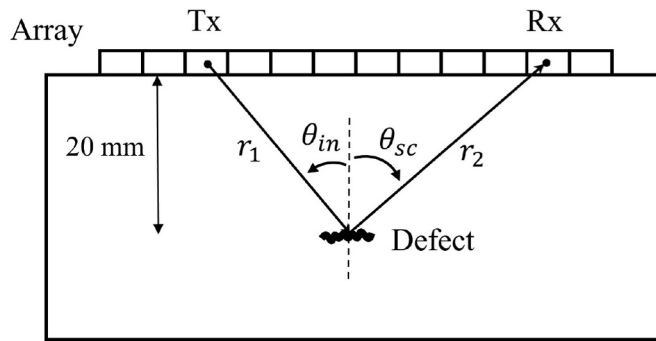


Fig. 1. Measurement configuration adopted in the simulation and experiments.

signal and data processing techniques, there is a fundamental limitation of the use of A-scan signals and ultrasonic images for characterization of sub-wavelength defects. Defect characterization based on the scattering matrix [26] is an alternative approach which has the potential to address this limitation. The scattering matrix can be extracted from the full matrix capture (FMC) data [12] and it contains information about the angular scattering behaviour of a defect. Zhang et al. showed that accurate crack sizing is achievable using the scattering matrix when the specular signal is measured and the size range is between 0.2 and 2 wavelengths [11]. Velichko et al. proposed a parametric manifold mapping approach as a generalization of the database searching method [27], and the effect of the distortion model on the characterization accuracy was studied in Ref. [28]. Compared to super-resolution imaging [29], the advantages of the scattering-matrix-based approaches include their capability to classify the defect types as well as to quantify the characterization uncertainty.

In this paper, we introduce the time-domain scattering matrix. Subsequently, we demonstrate its use in challenging inspection scenarios where the amplitude of the frequency-domain scattering matrix fails to achieve satisfactory characterization results because of a small defect size and/or unfavourable defect orientation. In such cases, the received signal amplitude is often small and the measurement is easily affected by noise, resulting in high characterization uncertainty [27]. For example, when a defect is very small (e.g. only a half of wavelength), sizing is still achievable based on the maximum amplitude of the scattering matrix. However, it is difficult to distinguish between different types of defects because of the small amplitude variation within the scattering matrix. The time-domain scattering matrix carries the amplitude and phase information of the scattering matrix over the entire frequency range covered by the input spectrum. Therefore, it is more suitable for classification of small crack-like defects and volumetric voids (regarded as less hazardous than cracks). However, time-domain scattering matrices extracted from experimental FMC data are dependent on the input signal and are sensitive to time shifts caused by localization errors. To address these problems which can limit the

practical application of the time-domain scattering matrix, we propose an approach for extracting shift-invariant features based on convolutional sparse coding (CSC) [30]. The performance improvement achieved by adopting this approach is demonstrated through characterization of rough cracks in a simulation. Furthermore, experiments were conducted using the proposed approach to characterize small horizontal defects and inclined crack-like defects. Excellent results were obtained in both cases.

2. Methodology

2.1. Time- and frequency-domain scattering matrices

The measurement configuration is shown in Fig. 1. A defect is located at a distance of 20 mm from the array center, and a 2.5 MHz, 64 element array with an element pitch of 0.5 mm is used in the simulation. The inspection material is assumed to be aluminium (Young's modulus = 69 GPa, Poisson's ratio = 0.334, and density = $2700 \text{ kg} \cdot \text{m}^{-3}$). By utilising the hybrid model of wave scattering developed in Ref. [11], the measured array data can be expressed as

$$G(x_T, x_R, \omega) = \frac{I_0(\omega)P(\theta_{in}, \omega)P(\theta_{sc}, \omega)\sqrt{\lambda}}{\sqrt{r_1 r_2}} \times \exp[ik(r_1 + r_2)] \times S(\theta_{in}, \theta_{sc}, \omega). \quad (1)$$

In Eq. (1), $I_0(\omega)$ is the spectrum of the input signal; $P(\cdot)$ denotes the element directivity function [10]; r_1 and r_2 are the distances from the transmitter and receiver elements (Tx, Rx) to the defect, respectively; $k = \omega/c$ is the wavenumber; and λ is the wavelength. The frequency-domain scattering matrix $S(\theta_{in}, \theta_{sc}, \omega)$ can be obtained from Eq. (1), and as its name suggests, it is a function of the incident angle θ_{in} , scattering angle θ_{sc} , and angular frequency ω . We can then define the time-domain scattering matrix as the inverse Fourier transform of $S(\theta_{in}, \theta_{sc}, \omega)$:

$$S(\text{Tx}, \text{Rx}, t) = \frac{1}{\pi} \int S(\theta_{in}, \theta_{sc}, \omega) e^{i\omega t} d\omega. \quad (2)$$

Note that only longitudinal waves were considered herein because the array measurements were performed in the direct contact mode without using wedges (see Fig. 1). The measured array data is normally the superposition of responses from many scatterers and structural features. Therefore, the extraction of the time-domain scattering matrix from the experimental data is not straightforward. Fig. 2 illustrates the defect characterization scheme proposed in this paper. A scattering matrix database is prepared by simulating the frequency-domain scattering matrices of the given type of defects using a finite element local scattering (FELS) model [31] and then by converting them into the time domain. The time-domain scattering matrices obtained in this way are termed the ‘theoretical’ scattering matrix in Fig. 2 and are used as the reference (training) data. In order to extract the time-domain scattering matrix from experimental data, a reversible imaging algorithm [32,33]

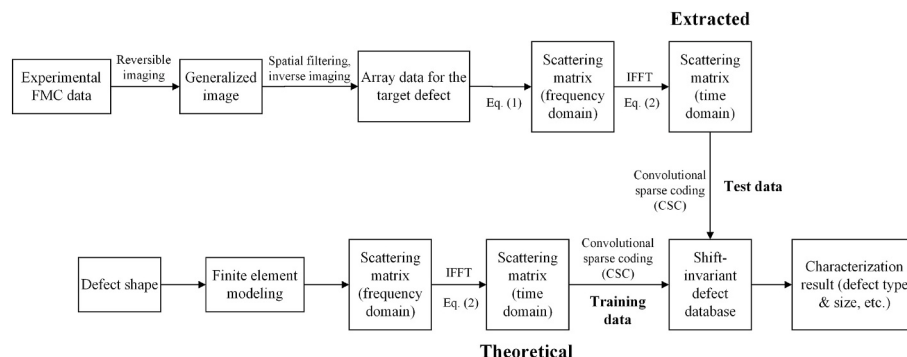


Fig. 2. Flowchart of the defect characterization approach based on the time-domain scattering matrix.

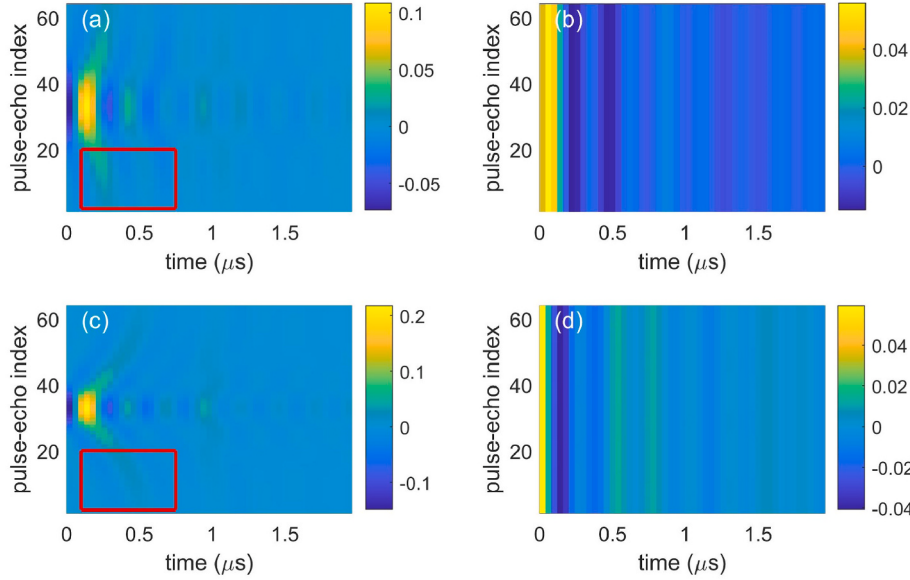


Fig. 3. Time-domain scattering matrices corresponding to the pulse-echo channels of the 64 element array adopted in the simulation and experiments: (a) 1.5 mm crack, (b) 1.5 mm hole, (c) 3 mm crack, and (d) 3 mm hole.

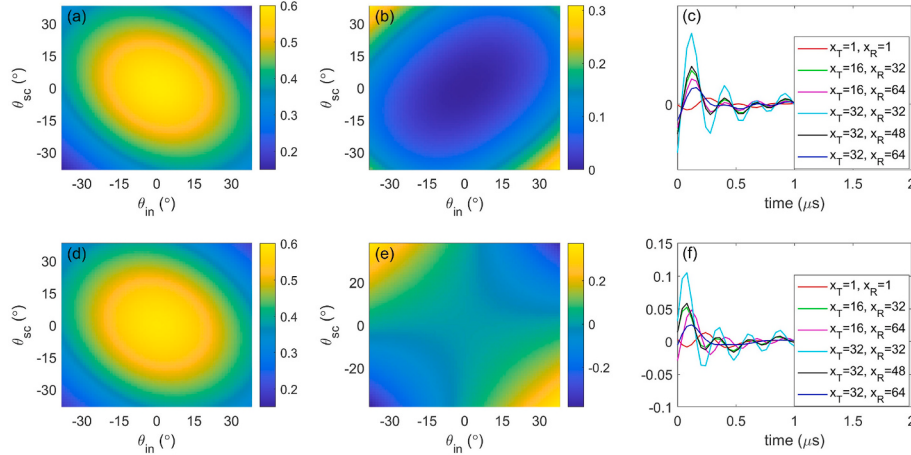


Fig. 4. Frequency-domain (amplitude and phase) and time-domain scattering matrices of a 1.5 mm crack (a–c) and a 1.5 mm ellipse with a width of 0.45 mm (d–f). Angular range of the scattering matrices in (a, b, d, and e) were determined from the measurement configuration shown in Fig. 1. (a, d) Amplitudes, and (b, e) phase angle results in radians. In (c) and (f), “Tx = 16, Rx = 32” refers to the A-scan measurement channel corresponding to the 16th transmitter element and the 32nd receiver element of the array.

can be applied first to extract the array data containing contributions only from the target defect using a spatial filtering approach. Alternatively, the FMC data of the target defect can be isolated from the original measurement data by subtracting interferences (*i.e.* “leaked energy”) of the nearby defects as described by Portzgen et al. in Ref. [34]. Next, Eq. (1) can be adopted to extract the frequency domain scattering matrices for frequencies up to a half of the sampling frequency f_s (25 MHz), from which the time-domain scattering matrix can be calculated. Interested readers are referred to Ref. [33] (and the supplemental material therein) for detailed descriptions about the reversible imaging approach and its delay-and-sum implementation.

Fig. 3(a)–(d) show the pulse-echo time-domain scattering matrices of a 1.5 mm crack, 1.5 mm hole, 3 mm crack, and 3 mm hole, respectively, assuming that the 2.5 MHz, 64 element array is used to perform the measurement (cracks are assumed to be horizontal). Both the amplitude and phase of different pulse-echo channels are seen to vary for cracks—the maximum amplitude of the scattering matrix is found when the incident wavefront is normal to the defect, and as the incident/scattering angle increases, the peak amplitude of an A-scan channel appears later in time compared to the normal-incident case. In comparison, the amplitude and phase remain unchanged for a hole across

different pulse-echo channels, which can be used to distinguish holes from crack-like defects. Note that the specular reflection signal may become unmeasurable for cracks having a large orientation angle. However, as will be discussed in Section 4, such cracks can still be sized accurately based on the phase information of the scattering matrix [see the diagonal patterns within the red boxes of Fig. 3(a) and (c) as an example].

As a simple illustration of the potential benefits of using the time-domain scattering matrix, Fig. 4 shows the time- and frequency-domain scattering matrices of a 1.5 mm crack and a 1.5 mm elliptical void which has a small width of 0.45 mm. Both defects are assumed to be horizontal, *i.e.*, they are parallel to the array direction as in Fig. 1. The term “frequency domain scattering matrix” is used hereafter to denote the amplitude of the scattering matrix $S(\theta_{in}, \theta_{sc}, \omega)$, as previous works have mostly been based on the amplitude and have often neglected the phase information [11,18,28]. Although a procedure was developed for using the phase difference within a scattering matrix, it assumed the scattering matrix independence at different frequencies, and hence, it could only be applied to a few discrete frequencies [35]. In contrast, the time-domain scattering matrix as defined in Eq. (2) provides an efficient way of using both the amplitude and phase parts of the scattering matrix

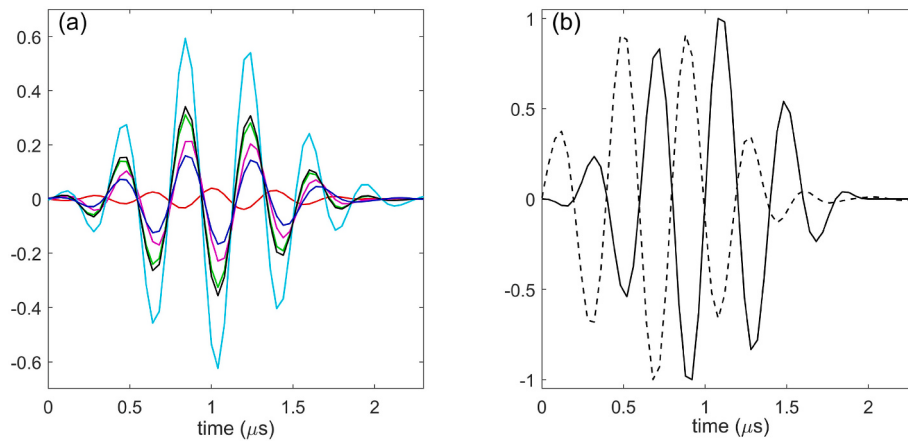


Fig. 5. (a) Time-domain scattering matrix of a 1.5 mm crack obtained using Eq. (3) where the input signal is a 5-cycle tone-burst [refer to Fig. 4(c) for the figure legend], (b) input signal (solid line) and learned waveform (dashed line) obtained with CSC.

for all available frequencies. The ultrasonic wavelength is 2.5 mm at the array center frequency in aluminium. Hence, the size of the crack and the volumetric defect considered here is only 0.6λ , which means that image-based characterization is fundamentally challenging [11]. Furthermore, we can observe from Fig. 4(a) and (d) that the frequency-domain scattering matrices of these defects show a small difference. Quantitatively, the relative Euclidean distance between the two scattering matrices defined as $\|S_{\text{crack}} - S_{\text{ellipse}}\|_2 / \|S_{\text{crack}}\|_2$ is only 2.76% ($\|\cdot\|_2$ denotes the Euclidean distance), and the correlation coefficient between them is 0.99, indicating a good match in shape and amplitude. However, the two defects are distinguishable if we compare their phases [Fig. 4(b) and (e)] and this is also reflected in their time-domain scattering matrices [Fig. 4(c) and (f)]. Note that the results for six representative A-scan channels are plotted in these figures and that the time-domain scattering matrix considered here contains $64 \times 64 = 4096$ such time signals. The relative Euclidean distance between the crack and the elliptical void calculated using the time-domain scattering matrix is 87.73%, and the correlation coefficient drops to 0.59. Hence, the time-domain scattering matrix carries additional information which can be used for more accurate characterization of these defects, as will be discussed in Section 3.

2.2. Convolutional sparse coding

In the development of the defect characterization procedure based on the framework shown in Fig. 2, it is important to consider that the time-domain scattering matrix extracted using the reversible imaging algorithm is related to the input spectrum. This is because when the scattering matrix is extracted from the experimental array data using Eq. (1), the effects of the beam spread and the element directivity can be modelled and compensated [10], but information about the input spectrum $I_0(\omega)$ often remains in the extraction result. In this case, the relationship between the experimentally extracted scattering matrix \tilde{s} (time domain), \tilde{S} (frequency domain), and theoretical frequency domain scattering matrix S can be expressed as

$$\tilde{s}(\text{Tx}, \text{Rx}, t) = \frac{1}{\pi} \int \tilde{S}(\theta_{in}, \theta_{sc}, \omega) e^{i\omega t} d\omega = \frac{1}{\pi} \int S(\theta_{in}, \theta_{sc}, \omega) I_0(\omega) e^{i\omega t} d\omega. \quad (3)$$

The effect of the input spectrum reduces to multiplication by a constant gain for the frequency-domain scattering matrix [26]. Hence, it is relatively easy to compensate for this effect and the normalization constant can usually be determined from the measurements of a reference reflector. However, this is not the case for the time-domain scattering matrices because in addition to the amplitude, the shape of the time signal is also affected by the input spectrum. Practically, this means that the scattering matrix database needs to be prepared following Eq.

(3) for the simulated data to be compared with the experimental measurements. Although this may be possible for certain applications, different scattering matrix databases are needed whenever a different UT system or simply a different array probe is used in experiments. Preparation of a scattering matrix database is a time-consuming task (in particular, when the number of the modelled defect types/sizes is large), and it is often conducted offline for this reason. As a result, the application of this technique in cases which require real-time inspection of a structure would be very difficult.

Another limitation of this approach (*i.e.* simulating the scattering matrix database using the input spectrum) is illustrated in Fig. 5. Fig. 5 (a) shows the time-domain scattering matrix of a 1.5 mm crack obtained with Eq. (3), and a 5-cycle tone-burst signal [solid line in Fig. 5(b)] is used here as the input signal. Compared with the result shown in Fig. 4 (c), it can be seen that there is an information loss (*e.g.* several peaks of close values as opposed to a single peak) caused by multiplying the band-limited input spectrum $I_0(\omega)$ and the theoretical scattering matrix S in the frequency domain. More importantly, registration of the time-series data (*e.g.* those obtained in the simulation and experiments) can become challenging because of the multiple peaks that have a small difference in value. Hence, the identification of the true peak is difficult in noisy environments.

To address the aforementioned difficulties, we propose an approach based on CSC for extracting deconvolved scattering matrix features that are robust to time-shifts. The CSC aims to solve the problem of dictionary learning [36] and is widely used in biomedical engineering owing to its ability to learn the morphologies of realistic signals such as electrophysiology signals [30,37]. Unlike the Fourier or wavelet transforms which use predefined bases with fixed shapes, CSC extracts waveforms (also termed ‘atoms’ [30]) based on a shift invariant sparse coding (SISC) model defined as [38].

$$\min_{d,z} \sum_{n=1}^N \left(\frac{1}{2} \left\| x_n - \sum_{l=1}^L d^l * z_n^l \right\|^2 + \lambda \sum_{l=1}^L \left\| z_n^l \right\|_1 \right), \text{ s.t. } \|d^l\|_2^2 \leq 1 \text{ and } z_n^l \geq 0, \forall n, l. \quad (4)$$

In Eq. (4), $x_n \in \mathbb{R}^K$ ($n = 1, 2, \dots, N$) are the original time signals of length K ; $d^l \in \mathbb{R}^M$ denotes the l -th atom of the learned dictionary; $z_n^l \in \mathbb{R}_+^{K-M+1}$ is called the activation of the l -th atom for signal x_n ; and $\|z\|_1$ is the L1-norm of z (*i.e.*, $\|z\|_1 = \sum_i |z_i|$). The convolution operation between d^l and z_n^l in Eq. (4) can explain the shift-invariance property of the CSC, and its sparsity is guaranteed by the L1 regularization term with $\lambda > 0$. The optimization problem defined in Eq. (4) can be solved by adopting a maximum a posteriori estimation procedure as follows [30]:

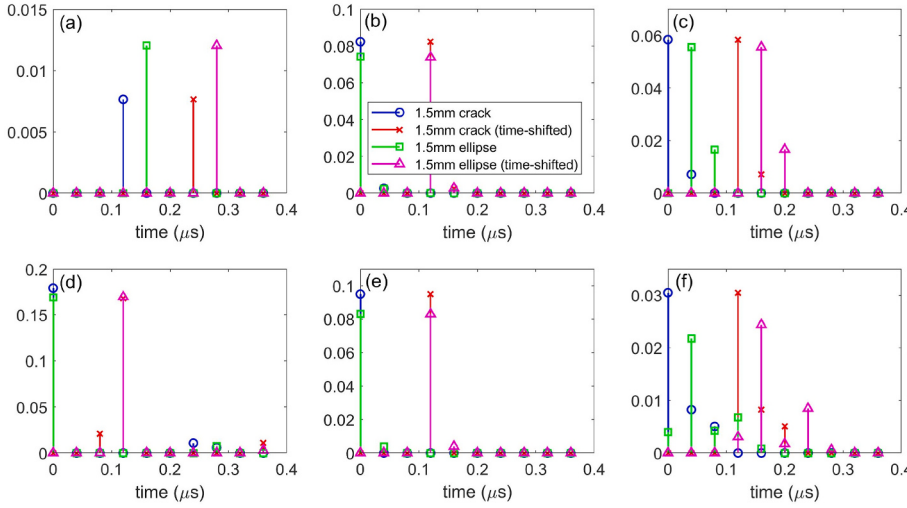


Fig. 6. Activations z_n [see Eq. (4)] of the time-domain scattering matrix of a 1.5 mm crack (blue and red) and a 1.5 mm ellipse (green and purple), where (a)–(f) show the results of the A-scan channels “Tx = 1, Rx = 1”, “Tx = 16, Rx = 32”, “Tx = 16, Rx = 64”, “Tx = 32, Rx = 32”, “Tx = 32, Rx = 48”, and “Tx = 32, Rx = 64”, respectively. The results shown in red and purple are obtained from the time-shifted scattering matrices of the crack and ellipse. (For interpretation of the references to colour in this figure legend, the reader is referred to the Web version of this article.)

$$(\tilde{d}, \tilde{z}) = \operatorname{argmax}_{d, z} \sum_{n,i} \left(\log p(x_{n,i}|d, z) + \sum_l \log p(z_{n,i}^l) \right). \quad (5)$$

In Eq. (5), the subscript i is used to denote the i -th element of a vector. It can also be shown that $(x_{n,i}|d, z)$ and $z_{n,i}^l$ follow the Gaussian and exponential distributions, respectively, from which the two probability terms of Eq. (5) can be calculated [30].

Although the time signals corresponding to different A-scan channels within a scattering matrix normally have different amplitudes and phases, they are all obtained in the simulation (and measured in experiments) with a single input signal. Therefore, the input signal can be retrieved using CSC, and more importantly, activations z_n can also be obtained which are deconvolved sparse representations of the time-domain scattering matrix. The dashed line in Fig. 5(b) shows the learned waveform d from the time-domain scattering matrix of a 1.5 mm crack [see Fig. 5(a)], where the number of atoms L is set to 1. The extracted waveform is observed to be consistent with the true input signal except for a phase difference. Nevertheless, the effect of this phase difference (or time-shift) is negligible because the learned atom d and

activation z are shift-invariant.

Fig. 6(a)–(f) show the activations z_n for the scattering matrices of a 1.5 mm crack (circles) and a 1.5 mm ellipse (squares) obtained with the regularization parameter $\lambda = 0.01$. Here, we set the lengths of the time-domain scattering matrix [x_n in Eq. (4)] and atom [d in Eq. (4)] to 100 and 91, respectively, and $z_n \in \mathbb{R}^{10}$ in this case (the time duration of the scattering matrix is 4 μ s). In order to study the effect of the time shift on the activation, the time-domain scattering matrix in Fig. 5(a) is shifted by 0.12 μ s (this corresponds to a localization error of 0.38 mm in aluminium). The corresponding activations \tilde{z} are shown as the crosses (crack) and triangles (ellipse) in Fig. 6. These results show that the activations \tilde{z}_n can indeed be obtained as the time-shifted version of z_n with a small error [e.g. see Fig. 6(d)] that is caused by partially discarding the signal when applying the time shift in the simulation. The value of the regularization parameter λ should be sufficiently large to provide sparse solutions to the optimization problem defined in Eq. (4). However, its selection should also be careful because the activation z_n can become 0 if λ exceeds a certain threshold [30].

The results in Figs. 5 and 6 have important implications in practice.

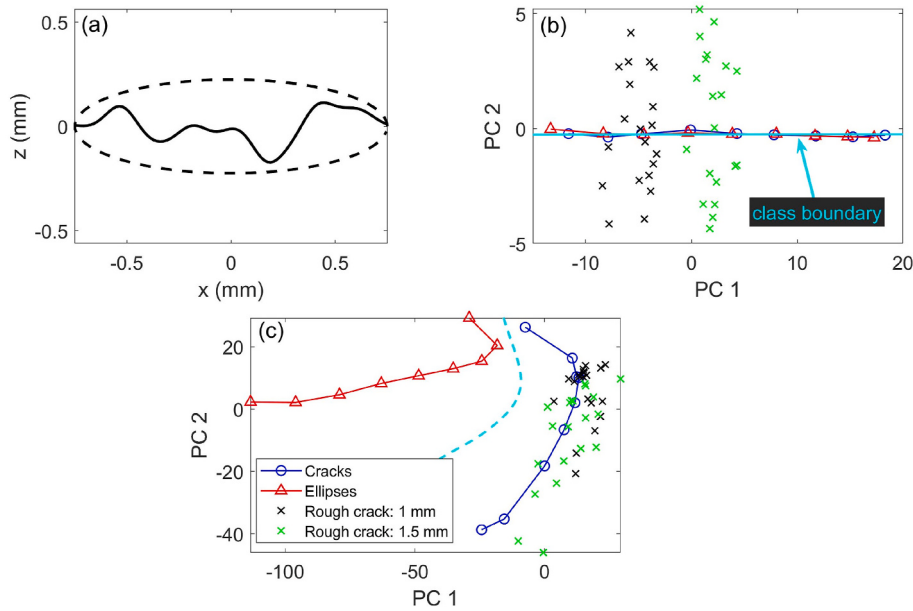


Fig. 7. (a) Shape of a 1.5 mm rough crack (solid line) and 1.5 mm ellipse (dashed line). (b–c) Distribution of the frequency-domain scattering matrices of the training and test samples in two-dimensional principal-component (PC) space using the amplitude and phase, respectively.

First, defect characterization can be performed based on the set of activations $Z \triangleq [z_1^T, z_2^T, \dots, z_N^T]^T$ instead of the time-domain scattering matrix [see Fig. 2]. $N = 4096$ is the number of the A-scan channels, and Z is referred to as the sparse-coded scattering matrix (SCSM) in the rest of this paper. Second, registration of the SCSM is straightforward because the activations z_n are sparse. In practice, all the activations z_n within an SCSM can be shifted by the same amount Δt , so that the first column of Z (*i.e.*, a vector which consists of $z_{n,1}$) is non-sparse. From Fig. 6, it can be seen that the original activations z_n (circles and squares) can be obtained from the time-shifted activations \tilde{z}_n (crosses and triangles) by adopting this approach, and this registration procedure is used for characterization of the simulation and experimental data in Sections 3 and 4.

3. Characterization of rough cracks

As described in Section 2.1, distinguishing a 1.5 mm ellipse with a small width from a 1.5 mm crack is difficult using the frequency-domain scattering matrix, but it can be achieved using its time-domain counterpart. In this section, the classification problem (of cracks and volumetric voids) is described further for the size range [0.5 mm, 2.5 mm] or equivalently, $[0.2\lambda, 1\lambda]$, using the time- and frequency-domain scattering matrices as well as the SCSM. Here, the training database consists of the cracks and ellipses [the width-to-length ratio of the ellipses is 0.3, see Fig. 7(a)] that have idealized smooth shapes. In addition, a test set was prepared using the simulated scattering matrices of 1 mm and 1.5 mm rough cracks [20 samples for each crack size, see Fig. 7(a) for an example shape of a rough crack]. The root-mean-squared (RMS) roughness and the correlation length of the rough cracks [29] were chosen as 75 μm and 100 μm , respectively, in the simulation. These values are consistent with those found from real thermal fatigue cracks and stress corrosion cracks [39,40]. The scattering matrices of the rough cracks were simulated using the finite element local scattering (FELS) model [31]. Only the vicinity of the defect region needs to be modelled using this approach, which enabled fast forward simulation of the test defects. In the FE model, the top and bottom rough surfaces were identical and they were symmetrically displaced around the mean surface [solid line in Fig. 7(a)]. The width of the rough crack was set to be 50 μm (equal to an FE element size), and more details about the adopted simulation process including the generation of the rough surface profiles can be found in Ref. [41].

Fig. 7(b) shows the scatter plot of the training and test samples after the PC application [21] to the dataset of the frequency-domain scattering matrices. It can be seen from this result that cracks and ellipses are largely overlapped in the PC space with a small margin. Thus, only their sizing can be achieved in this case (*e.g.* using the value of ‘PC 1’). The size of the rough cracks shown as the crosses can be determined by adopting the nearest neighbour method or a statistical Bayesian approach [18]. However, the classification of the rough cracks is challenging, which can potentially lead to the underestimation of the severity of a defect. The cyan line in Fig. 7(b) shows the class boundary obtained using a support vector machine (SVM) classifier with a linear kernel [42]. The classification accuracy is only 50% for the rough cracks shown as the crosses based on this result. As a comparison, Fig. 7(c) shows the distribution of the training and test samples when the phase of the scattering matrix is used for characterization. The database cracks and ellipses are seen to be separable in this result, where the decision boundary (dashed line) is obtained using an SVM classifier with a Gaussian kernel. It is noted that the phase result is dependent on the reference point with respect to which it is extracted [35]. In this paper, the reference point is chosen as the coordinate origin [see Fig. 7(a)] which is the geometric centre of an idealized defect. However, the actual geometric centre may be different for the rough cracks, and a systematic alignment procedure is needed in practice for characterization of realistic defects with irregular shapes. For this reason, sizing errors of the rough cracks are relatively large if we use the phase information directly

Table 1

Sizing results of 1 mm and 1.5 mm rough cracks (mean \pm one standard deviation, in millimeters), obtained using different scattering matrix representations.

Scattering matrix	1 mm cracks	1.5 mm cracks
Frequency domain (amplitude)	0.95 ± 0.10	1.36 ± 0.13
Frequency domain (phase)	1.36 ± 0.24	1.70 ± 0.31
Time domain	1.55 ± 0.38	2.00 ± 0.37
SCSM	1.03 ± 0.08	1.54 ± 0.10

for their characterization (see Table 1).

Fig. 8(a) shows the scatter plot result when the time-domain scattering matrices are used for characterization. Similarly to Fig. 7(b), the database cracks and ellipses are well separated in this result, and the dashed line shows the decision boundary given by a linear SVM. The rough cracks (crosses) can be correctly classified based on this result, demonstrating the benefits of using the time-domain scattering matrix. However, the time-shifted scattering matrices of the rough cracks (squares that are obtained with a time shift $\Delta t = 0.12 \mu\text{s}$) are either incorrectly classified as ellipses by the SVM, or are simply identified as “out of database” defects because of the large distances from the reference cracks and ellipses [23]. Moreover, accurate sizing is difficult (*e.g.*, distinguishing between 1 mm and 1.5 mm rough cracks) by using the original time-domain scattering matrix, and this is believed to be caused by a lack of time alignment between the training and test samples.

The database cracks and ellipses remain separable in terms of the SCSM, as shown in Fig. 8(b). By adopting the registration procedure described in Section 2.2, we find that the SCSMs extracted from the time-shifted and original time-domain scattering matrices of the rough cracks (squares and crosses) are clustered within the same region, and 1 mm and 1.5 mm rough cracks are well separated in the PC space. Table 1 summarises the mean and standard deviation of the sizing results obtained with the k-nearest neighbour approach ($k = 1$) [43] based on the results shown in Figs. 7 and 8. In conclusion, the use of the SCSM improves the classification performance of the rough cracks, and it also preserves (or marginally improves) the sizing accuracy of the frequency domain scattering matrix (mean sizing errors are reduced by 0.02 mm and 0.1 mm for 1 mm and 1.5 mm rough cracks, respectively). Hence, the SCSM contains information useful for improving the characterization accuracy and its extraction is robust to time shifts, making it an ideal choice for characterization of realistic defects such as rough cracks.

4. Experimental results

The characterization performance of the proposed approach based on the SCSM was further studied in two experimental cases [see Fig. 9 (a)–(b), the sample material is aluminium]. A 2.5 MHz, 64 element array with an element pitch of 0.5 mm was used as in the simulation, and defects in Fig. 9(a)–(b) were manufactured using wire electrical discharge machining. The frequency domain scattering matrix was extracted from the experimental data using the reversible imaging algorithm, and then the time-domain scattering matrix was computed using Eq. (2) [see Fig. 2]. Note that the same measurement configuration as in Fig. 1 was adopted in all experiments (*i.e.* the defect is located at the array center).

4.1. Characterization of small horizontal defects

The two defects in Fig. 9(a) have the same size of 1.5 mm (0.6λ at the array center frequency), and the widths of the slot and elliptical defect are 0.35 mm and 0.6 mm, respectively. It is shown in Section 2.1 that the frequency-domain scattering matrices perform poorly for distinguishing such small crack-like defects from volumetric voids, and here, we only consider using the SCSM for their characterization.

Fig. 10(a)–(b) show the SCSMs obtained in the simulation for a 1.5 mm crack and a 1.5 mm ellipse. Note here that half matrix capture

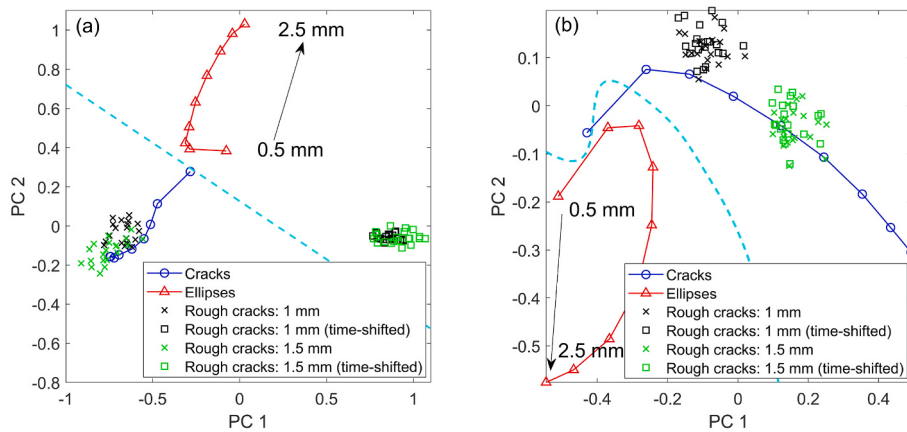


Fig. 8. Scatter plots of the training and test samples obtained with (a) the time-domain scattering matrix and (b) the SCSM.

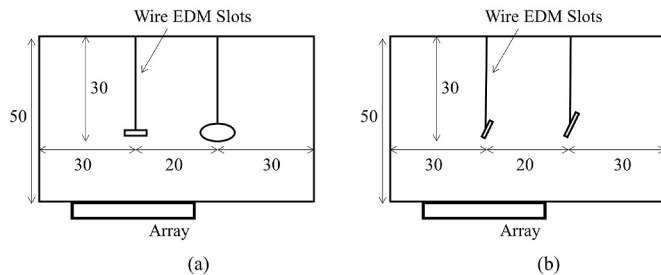


Fig. 9. Aluminium specimens used in the experiments. The specimens contain (a) a horizontal slot and an elliptical defect and (b) two inclined (60°) slots. Dimensions are in millimeters.

(HMC) is assumed in the simulation (and adopted in experiments). Hence, A-scan channels 1, 2, ..., 2080 correspond to “Tx = 1, Rx = 1”, “Tx = 1, Rx = 2”, ..., “Tx = 64, Rx = 64” in these results. It can be seen that the SCSM of the ideal crack has non-zero components mainly at Z_1 (the first column of Z , corresponding to $t = 0$), whereas the SCSM of the

ellipse is non-sparse also for Z_2 and Z_3 (the second and third columns of Z , corresponding to $t = 0.04$ and $t = 0.08 \mu\text{s}$, respectively). In addition, the indices of the non-zero components of Z_i ($i = 1, 2$, and 3) exhibit an upward shift in Fig. 10(b). Fig. 10(c)–(d) show experimentally measured SCSMs for the slot and the elliptical defect. Although both results appear to have two non-sparse columns, Z_2 of the crack SCSM can be neglected compared to that of the ellipse. For the experimentally measured SCSM of the ellipse, Z_1 and Z_2 also show a similar shift pattern to those in Fig. 10(b). The difference found for the simulated [Fig. 10(a)–(b)] and experimental [Fig. 10(c)–(d)] SCSMs is related to the difference between the theoretical and extracted time-domain scattering matrices, as discussed in Section 2.2. Hence, this result also reveals a limitation of the proposed defect characterization scheme shown in Fig. 2—as the bandwidth of the input spectrum reduces, the match between the training and measured data could become poor even after the sparse encoding. In practice, the bandwidth of the transducer array needs to be sufficiently large in order to achieve a high characterization accuracy.

The -6 dB bandwidth of the 2.5 MHz array used in experiments is [1.5, 3.5] MHz. Based on the results in Fig. 10, defect characterization can be performed by comparing the SCSMs measured in the experiments

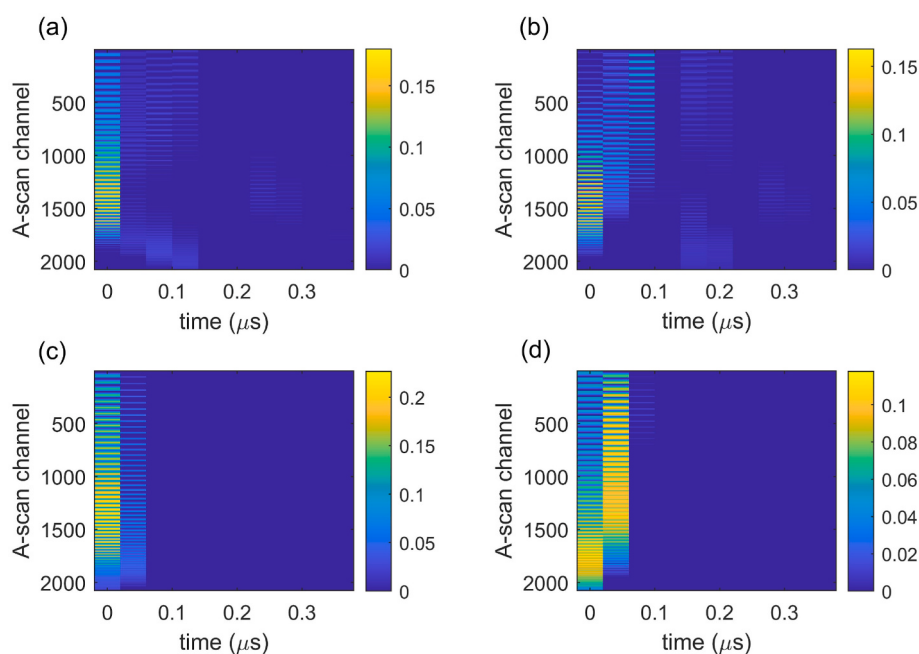


Fig. 10. SCSMs of a 1.5 mm crack and 1.5 mm ellipse obtained in the simulation and experiments, where (a) crack, simulation; (b) ellipse, simulation; (c) crack, experiment; and (d) ellipse, experiment.

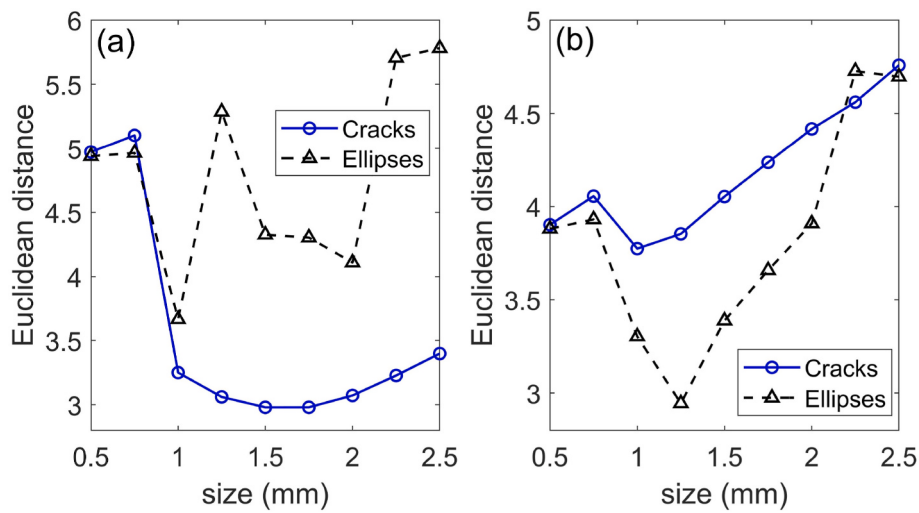


Fig. 11. The Euclidean distances between the experimentally measured SCSMs and those of the reference defects, showing the results of (a) the 1.5 mm slot, and (b) the 1.5 mm ellipse.

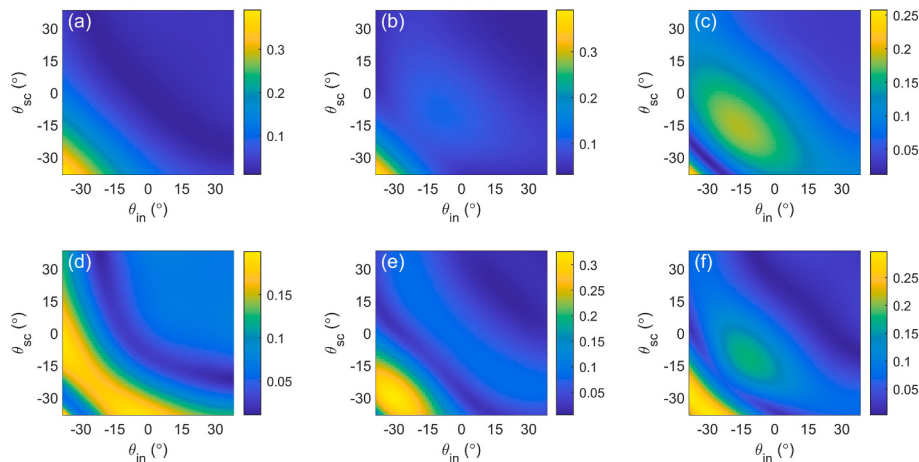


Fig. 12. Frequency-domain scattering matrices of 60° cracks having different sizes, where (a) 1.5 mm, (b) 2 mm, (c) 2.5 mm, (d) 3 mm, (e) 3.5 mm, and (f) 4 mm.

with those obtained in the simulation for idealized reference defects. The size range of the reference defects considered here is between 0.5 mm (0.2λ) and 2.5 mm (1λ), and all the modelled ellipses have the same width-to-length ratio. Fig. 11(a)-(b) show the Euclidean distances between the SCSMs extracted from the experimental data and the simulated SCSMs. From this result, the characterization result can be obtained as the reference defect which has the minimum distance to the experimental data. In Fig. 11(a), the minimum distance is found for the

cracks having sizes 1.5 mm and 1.75 mm, and hence, the slot can be sized to within 0.25 mm. The minimum distance is found for the 1.25 mm ellipse in Fig. 11(b), and the sizing error is 0.25 mm for the elliptical defect. In addition, these results demonstrate accurate classification with a high confidence, because the difference between the minimum distances of the ‘correct’ and ‘wrong’ defect classes is large in both cases.

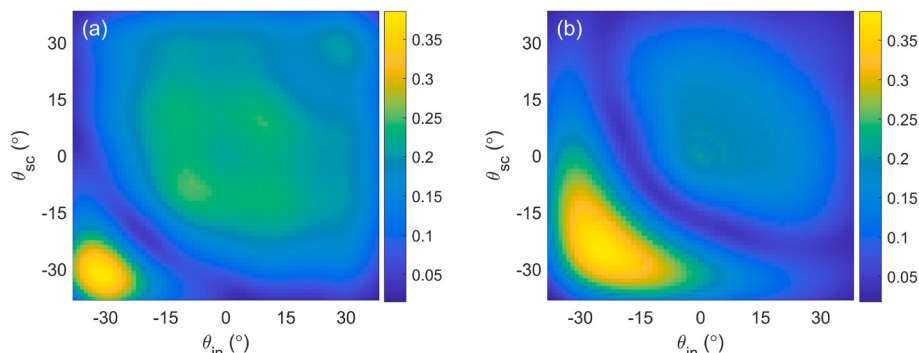


Fig. 13. Experimentally measured frequency-domain scattering matrices of a (a) 2 mm slot and (b) 3 mm slot.

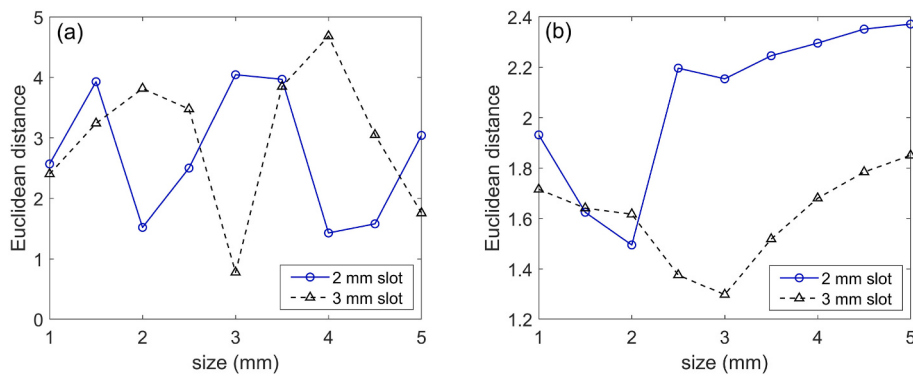


Fig. 14. Euclidean distances between the experimental measurements of the inclined slots and the reference cracks, where (a) the frequency-domain scattering matrix and (b) the SCSM, are used for characterization.

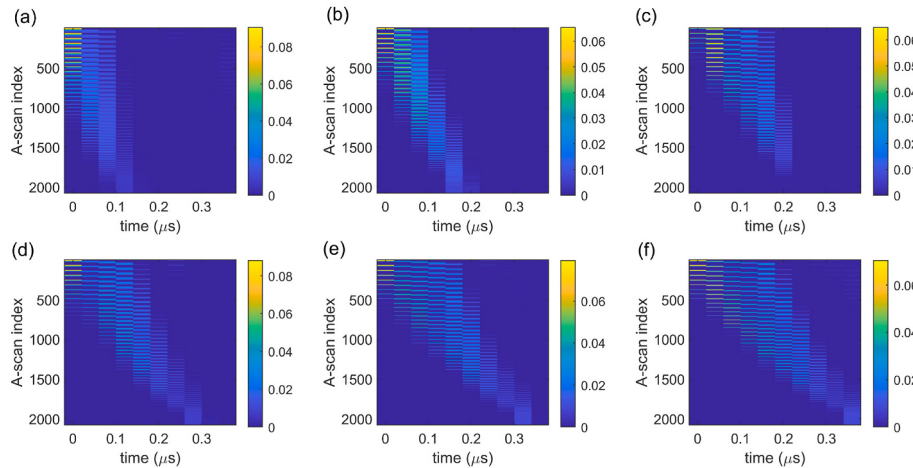


Fig. 15. SCSMs of 60° cracks having different sizes, where (a) 1.5 mm, (b) 2 mm, (c) 2.5 mm, (d) 3 mm, (e) 3.5 mm, and (f) 4 mm.

4.2. Sizing of inclined crack-like defects

In addition to the classification of the defect type for small cracks and volumetric voids, the SCSM can also be used for sizing of inclined cracks. The received signal amplitude is often very small for such unfavourably oriented cracks regardless of their sizes, and in this case, direct application of amplitude-based techniques can result in high characterization uncertainty [27]. Fig. 12(a)-(f) show the frequency-domain scattering matrices obtained in a simulation for 60° cracks of sizes between 1.5 mm (0.6λ) and 4 mm (1.6λ). The orientation angle of a crack is defined with respect to the array direction and the modelled frequency is 2.5 MHz. Although the size range considered here is relatively large, it can be

observed that the scattering matrices in Fig. 12 have similar peak amplitudes (around 0.3). These amplitudes are significantly lower than the horizontal crack and ellipse with a size of 1.5 mm [see Fig. 4(a)-(b)]. Moreover, the shape patterns of these scattering matrices are similar (e.g. peak amplitude found at the left bottom corner), and hence, distinctive features cannot be extracted (e.g. using PCA) from these results on the defect sizing.

The size of the two inclined slots shown in Fig. 9(b) are 2 mm (0.8λ) and 3 mm (1.2λ), respectively, and Fig. 13(a)-(b) are experimentally measured scattering matrices of the two defects. The nearest neighbour approach was adopted for their characterization, and the results are shown in Fig. 14(a). The size of the 2 mm slot would be incorrectly

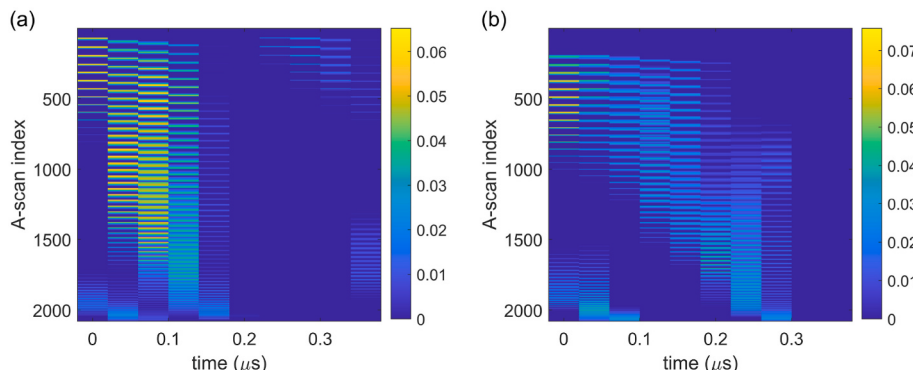


Fig. 16. Experimentally measured SCSMs of a (a) 2 mm slot and (b) 3 mm slot.

identified as 4 mm based on this result [see the solid line in Fig. 14(a)]. In fact, the distances between the 2 mm, 4 mm, and 4.5 mm cracks and the experimental data are quite similar, which suggests that the characterization uncertainty is inherently high for this defect. Although the size of the 3 mm slot is determined accurately [see the dashed line in Fig. 14(a)], the distance between the 5 mm crack and the experimental data is small, and the characterization result can potentially become unstable in noisy environments.

Fig. 15(a)-(f) show the SCSMs of the simulated cracks which have sizes between 1.5 mm and 4 mm, and the experimentally measured SCSMs of the two slots are shown in Fig. 16(a)-(b). It is straightforward to distinguish the inclined cracks of different sizes based on the results in Fig. 15 because the number of the non-sparse columns of the SCSM increases with the crack size. For the inclined cracks, the phase part of the scattering matrix carries critical information, and if a crack is sufficiently large, the TOFD method can be used for sizing. As shown in Figs. 15 and 16, the phase information of the scattering matrix can still be encoded in the SCSM even when the crack size is small (e.g. below 1λ). Fig. 14(b) shows the characterization results obtained for the two inclined slots using the nearest neighbour approach, and both defects are accurately sized based on the SCSM. The solid and dashed lines in Fig. 14(b) only have a global minimum as opposed to the results in Fig. 14(a), and these sizing results are thus expected to be more robust to the measurement noise.

5. Conclusions

In this paper, the use of the time-domain scattering matrix was investigated for defect characterization. The time-domain scattering matrix is particularly useful for cases in which the frequency-domain scattering matrix fails to provide sufficient characterization information. However, the experimentally measured time-domain scattering matrix is sensitive to time-shifts caused by localization errors. To address this problem, we propose an approach based on CSC for extracting shift-invariant features of the time-domain scattering matrix. By adopting this approach, feature extraction can be performed separately for reference defects and experimental data. Defect characterization can be then conducted using the extracted features (SCSMs) that are independent of the input spectrum.

A simulation was conducted to demonstrate the use of the SCSM for characterization of rough cracks. Compared to the frequency-domain scattering matrix, the SCSM improved the classification performance of the rough cracks and the sizing accuracy. In experiments, the SCSM was used for sizing inclined crack-like defects, and the results were shown to be accurate with a high confidence. The proposed approach can be easily integrated into existing inspection systems as the SCSM can be extracted from the FMC data and no additional data acquisition procedure is required. An NDE operator is free to choose (or develop) the appropriate characterization approach based on the SCSM, including the application of advanced machine learning and deep learning algorithms given that sufficient training data are available. The database of the reference defects can also be extended to include different types of defects, including inclusions and porosity. These aspects of the work will be covered in our future research.

CRediT author statements

L. Bai: Conceptualization, Methodology, Software, Validation, Formal analysis, Investigation, Writing - Original Draft, Writing - Review & Editing, Visualization, Funding acquisition.

N. Liu: Methodology, Writing - Original Draft, Investigation, Resources.

C. Guo: Methodology, Software, Writing - Original Draft.

J. Xu: Conceptualization, Writing - Original Draft, Writing - Review & Editing, Project administration, Funding acquisition.

Declaration of competing interest

The authors declare that they have no known competing financial interests or personal relationships that could have appeared to influence the work reported in this paper.

Acknowledgement

This work was supported by National Natural Science Foundation of China under grant number 52005205.

References

- [1] Kundu T. Ultrasonic nondestructive evaluation: engineering and biological material characterization. Boca Raton, FL: CRC Press; 2004.
- [2] Achenbach JD. Quantitative nondestructive evaluation. Int J Solid Struct 2000;37(1-2):13-27. [https://doi.org/10.1016/S0020-7683\(99\)00074-8](https://doi.org/10.1016/S0020-7683(99)00074-8).
- [3] Lanza di Scalea F, Rizzo P, Coccia S, Bartoli I, Fateh M, Viola E, Pascale G. Non-contact ultrasonic inspection of rails and signal processing for automatic defect detection and classification. Insight 2005;47(6):346-53. <https://doi.org/10.1784/insl.47.6.346.66449>.
- [4] Shakibi B, Honarvar F, Moles MD, Caldwell J, Sinclair AN. Resolution enhancement of ultrasonic defect signals for crack sizing. NDT E Int 2012;52:37-50. <https://doi.org/10.1016/j.ndteint.2012.08.003>.
- [5] Song SJ, Shin HJ, Jang YH. Development of an ultrasonic phased array system for nondestructive tests of nuclear power plant components. Nucl Eng Des 2002;214(1-2):151-61. [https://doi.org/10.1016/S0029-5493\(02\)00024-9](https://doi.org/10.1016/S0029-5493(02)00024-9).
- [6] Honarvar F, Varyani-Farahani A. A review of ultrasonic testing applications in additive manufacturing: defect evaluation, material characterization, and process control. Ultrasonics 2020;108:106227. <https://doi.org/10.1016/j.ultras.2020.106227>.
- [7] Brierley N, Tippett T, Cawley P. Data fusion for automated non-destructive inspection. Proc R Soc A 2014;470(2167):20140167. <https://doi.org/10.1098/rspa.2014.0167>.
- [8] Blitz J, Simpson G. Ultrasonic methods of non-destructive testing. London, UK: Chapman & Hall; 1996.
- [9] Sinclair AN, Fortin J, Shakibi B, Honarvar F, Jastrzebski M, Moles MDC. Enhancement of ultrasonic images for sizing of defects by time-of-flight diffraction. NDT E Int 2010;43(3):258-64. <https://doi.org/10.1016/j.ndteint.2009.12.003>.
- [10] Drinkwater BW, Wilcox PD. Ultrasonic arrays for non-destructive evaluation: a review. NDT E Int 2006;39(7):525-41. <https://doi.org/10.1016/j.ndteint.2006.03.006>.
- [11] Zhang J, Drinkwater BW, Wilcox PD. The use of ultrasonic arrays to characterize crack-like defects. J Nondestr Eval 2010;29(4):222-32. <https://doi.org/10.1007/s10921-010-0080-6>.
- [12] Holmes C, Drinkwater BW, Wilcox PD. Post-processing of the full matrix of ultrasonic transmit-receive array data for nondestructive evaluation. NDT E Int 2005;38(8):701-11. <https://doi.org/10.1016/j.ndteint.2005.04.002>.
- [13] Camacho J, Atehortua D, Cruza JF, Brizuela J, Ealo J. Ultrasonic crack evaluation by phase coherence processing and TFM and its application to online monitoring in fatigue tests. NDT E Int 2018;93:164-74. <https://doi.org/10.1016/j.ndteint.2017.10.007>.
- [14] Ménard C, Robert S, Miorelli R, Lesselier D. Optimization algorithms for ultrasonic array imaging in homogeneous anisotropic steel components with unknown properties. NDT E Int 2020;116:1102327. <https://doi.org/10.1016/j.ndteint.2020.102327>.
- [15] Lin L, Cao H, Luo Z. Total focusing method imaging of multidirectional CFRP laminate with model-based time delay correction. NDT E Int 2018;97:51-8. <https://doi.org/10.1016/j.ndteint.2018.03.011>.
- [16] Goodfellow I, Bengio Y, Courville A. Deep learning. Cambridge, MA: MIT Press; 2017.
- [17] Munir N, Kim HJ, Park J, Song SJ, Kang SS. Convolutional neural network for ultrasonic weldment flaw classification in noisy conditions. Ultrasonics 2019;94:74-81. <https://doi.org/10.1016/j.ultras.2018.12.001>.
- [18] Bai L, Le Bourdais F, Miorelli R, Calmon P, Velichko A, Drinkwater BW. Ultrasonic defect characterization using the scattering matrix: a performance comparison study of Bayesian inversion and machine learning schemas. IEEE Trans Ultrason Ferroelectr Freq Control 2021;68(10):3143-55. <https://doi.org/10.1109/TUFFC.2021.3084798>.
- [19] Pyle RJ, Bevan RLT, Hughes RR, Rachev RK, Ali AAS, Wilcox PD. Deep learning for ultrasonic crack characterization in NDE. IEEE Trans Ultrason Ferroelectrics Freq Control 2021;68(5):1854-65. <https://doi.org/10.1109/TUFFC.2020.3045847>.
- [20] Munir N, Park J, Kim HJ, Song SJ, Kang SS. Performance enhancement of convolutional neural network for ultrasonic flaw classification by adopting autoencoder. NDT E Int 2020;111:102218. <https://doi.org/10.1016/j.ndteint.2020.102218>.
- [21] Jolliffe IT. Principal component analysis. second ed. New York, NY: Springer-Verlag; 2002.
- [22] Cruz FC, Simas Filho EF, Albuquerque MCS, Silva IC, Farias CTT, Gouvêa LL. Efficient feature selection for neural network based detection of flaws in steel welded joints using ultrasound testing. Ultrasonics 2017;73:1-8. <https://doi.org/10.1016/j.ultras.2016.08.017>.

- [23] Bai L, Velichko A, Drinkwater BW. Characterization of defects using ultrasonic arrays: a dynamic classifier approach. *IEEE Trans Ultrason Ferroelectrics Freq Control* 2015;62(12):2146–60. <https://doi.org/10.1109/TUFFC.2015.007334>.
- [24] Oliveira MA, Simas Filho EF, Albuquerque MCS, Santos YTB, da Silva IC, Farias CTT. Ultrasound-based identification of damage in wind turbine blades using novelty detection. *Ultrasonics* 2020;108:106166. <https://doi.org/10.1016/j.ultras.2020.106166>.
- [25] Gao F, Li B, Chen L, Shang Z, Wei X, He C. A softmax classifier for high-precision classification of ultrasonic similar signals. *Ultrasonics* 2021;112:106344. [10.1016/j.ultras.2020.106344](https://doi.org/10.1016/j.ultras.2020.106344).
- [26] Zhang J, Drinkwater BW, Wilcox PD. Defect characterization using an ultrasonic array to measure the scattering coefficient matrix. *IEEE Trans Ultrason Ferroelectrics Freq Control* 2008;55(10):2254–65. <https://doi.org/10.1109/TUFFC.924>.
- [27] Velichko A, Bai L, Drinkwater BW. Ultrasonic defect characterization using parametric-manifold mapping. *Proc R Soc A* 2017;473(2202):20170056. <https://doi.org/10.1098/rspa.2017.0056>.
- [28] Bai L, Velichko A, Clare AT, Dryburgh P, Pieris D, Drinkwater BW. The effect of distortion models on characterisation of real defects using ultrasonic arrays. *NDT E Int* 2020;113:102263. <https://doi.org/10.1016/j.ndteint.2020.102263>.
- [29] Elliott JB, Lowe MJS, Huthwaite P, Phillips R, Duxbury DJ. Sizing subwavelength defects with ultrasonic imagery: an assessment of super-resolution imaging on simulated rough defects. *IEEE Trans Ultrason Ferroelectrics Freq Control* 2019;66(10):1634–48. <https://doi.org/10.1109/TUFFC.2019.2925974>.
- [30] Jas M, Dupré La Tour T, Simsekli U, Gramfort A. Learning the morphology of brain signals using alpha-stable convolutional sparse coding. *Adv Neural Inf Process Syst* 2017;1099–108.
- [31] Velichko A, Wilcox PD. A generalized approach for efficient finite element modelling of elastodynamic scattering in two and three dimensions. *J Acoust Soc Am* 2010;128(3):1004–14. <https://doi.org/10.1121/1.3467775>.
- [32] Velichko A, Wilcox PD. Reversible back-propagation imaging algorithm for postprocessing of ultrasonic array data. *IEEE Trans Ultrason Ferroelectrics Freq Control* 2009;56(11):2492–503.
- [33] Velichko A, Villaverde EL, Croxford AJ. Local scattering ultrasound imaging. *Sci Rep* 2021;11:993. <https://doi.org/10.1038/s41598-020-79617-z>.
- [34] Portzgen N, Gisolf D, Verschuur DJ. Wave equation-based imaging of mode converted waves in ultrasonic NDI, with suppressed leakage from nonmode converted waves. *IEEE Trans Ultrason Ferroelectrics Freq Control* 2008;55(8):1768–80. <https://doi.org/10.1109/TUFFC.2008.861>.
- [35] Bai L, Velichko A, Drinkwater BW. Ultrasonic defect characterisation-Use of amplitude, phase, and frequency information. *J Acoust Soc Am* 2018;143(1):349–60. <https://doi.org/10.1121/1.5021246>.
- [36] Brockmeier AJ, Principe JC. Learning recurrent waveforms within EEGs. *IEEE Trans Biomed Eng* 2016;63(1):43–54. <https://doi.org/10.1109/TBME.2015.2499241>.
- [37] Dupré La Tour T, Moreau T, Jas M, Gramfort A. Multivariate convolutional sparse coding for electromagnetic brain signals. In: *Advances in Neural Information Processing System (NeurIPS)*; 2018. p. 3296–306.
- [38] Grossé R, Raina R, Kwong H, Ng AY. Shift-invariant sparse coding for audio classification. In: in: *Conference on Uncertainty in Artificial Intelligence (UAI)*; 2007.
- [39] Wåle J, Ekström P. Crack characterization for in-service inspection planning. Stockholm, Sweden: Technical Report, SKI, SAQ Inspection; 1995. SAQ-FOUC95-70.
- [40] Wåle J. Crack characterisation for in-service inspection planning-An update. Stockholm, Sweden: Technical Report, SKI, Swedish Nucl. Power Inspectorate; 2006. SKI-R-06-24.
- [41] Zhang J, Drinkwater BW, Wilcox PD. Effect of roughness on imaging and sizing rough crack-like defects using ultrasonic arrays. *IEEE Trans Ultrason Ferroelectrics Freq Control* 2012;59(5):939–48. <https://doi.org/10.1109/TUFFC.2012.2278>.
- [42] Chang CC, Lin CJ. LIBSVM: a library for support vector machines. *ACM Trans Intell Syst Technol* 2011;2(3):1–27. <https://doi.org/10.1145/1961189.1961199>.
- [43] Cover T, Hart P. Nearest neighbor pattern classification. *IEEE Trans Inf Theor* 1967;13(1):21–7. <https://doi.org/10.1109/TIT.1967.1053964>.